Supplementary Information

Nonlinear Metamaterials Enhanced Surface Coil Array for Parallel Magnetic Resonance Imaging

Bingbai Li,[1] Rongbo Xie,[1] Zhenci Sun,[1] Xin Shao,[2] Yuan Lian,[2] Hua Guo,[2] Rui You,[3,*] Zheng You,[1,4,*] and Xiaoguang Zhao[1,4,*]

[1] Department of Precision Instrument, Tsinghua University, Beijing, 100084, China.

[2] Center for Biomedical Imaging Research, Department of Biomedical Engineering, School of Medicine, Tsinghua University, Beijing, 100084, China.

[3] School of Instrument Science and Opto-electronics Engineering, Beijing Information Science and Technology University, Beijing, 100192, China.

[4] Beijing Advanced Innovation Center for Integrated Circuits, Beijing, 100084, China.

*Correspondence: yourui@bistu.edu.cn (R. Y.); yz-dpi@mail.tsinghua.edu.cn (Z. Y.); zhaoxg@mail.tsinghua.edu.cn (X. Z.)

S1. Design of the nonlinear meta-atom

The metamaterial design in this study inherits from previous works [S1] and [S2]. We determined to optimize the structure by integrating VLSRRs (varactor loaded split ring resonators) into each meta-atom, according to the estimation of the coupling effect between VLSRR and coil element in the surface coil array. Specifically, we simplified the coil element and the VLSRR as two coaxial loops and calculate the mutual inductance between them using the Maxwell Formula[S3]:

$$c = \frac{2\sqrt{Rr}}{\sqrt{(R+r)^2 + \Delta^2}} \tag{1-1}$$

$$M = -\mu_0\sqrt{Rr}\left(\left(c - \frac{2}{c}\right)K(c) + \frac{2}{c}E(c)\right) \tag{1-2}$$

where R and r represent the radii of the two loops, Δ is the distance between them, and K and E are elliptic integrals of c. We set R=60 mm which is similar to the size of conventional RF coils or the VLSRR in previous studies, and calculate the mutual inductance under various r and Δ. The results are shown in Supplementary Fig. 1a. We observed a significant intensification of coupling when the size of the VLSRR approaches that of the coil element, which suggests a potential for interference with the surface coil. To improve compatibility between the VLSRR and the surface coils, we determined to introduce a small VLSRR to each meta-atom, forming the nonlinear meta-atom (NMA).

Additionally, concerning additional losses caused by employing more lumped elements- varactors, we theoretically and experimentally found that dielectric loss dominates losses in the meta-atom, and the integration of VLSRRs into each NMA results in a slight decrease in the quality factor. Specifically, the internal resistance of the varactor (SMV1235-079LF, Skyworks) is 0.60Ω (measured at 500MHz, 3V bias, as per the datasheet). Then we access the ohmic and dielectric losses in the solenoid part[S1] of the nonlinear meta-atom (NMA):

$$R_{ohm} = \sqrt{\frac{\omega_0 \mu_0 \rho}{2}} \frac{l_{w,tot}}{\pi d} = 0.818\,\Omega \tag{1-3}$$

$$R_{dielec} = \frac{2\varepsilon_{im}}{\omega_0 C(\varepsilon_{re}+1)^2} = \frac{2\varepsilon_{im}\omega_0 L}{(\varepsilon_{re}+1)^2} = 15.8\,\Omega \tag{1-4}$$

The geometric parameters of the solenoid are detailed in Supplementary Table 1, and ρ is the resistivity of copper, ε=2+0.06i is the permittivity of the scaffold's material, and ω_0=143 MHz is the resonant frequency of the single solenoid. The solenoid inductance L is calculated using the Nagaoka formula[S4]:

$$L = \frac{\pi \mu_0 N^2 D^2}{4l} F\left(\frac{D}{l}\right) \tag{1-5}$$

$$F\left(\frac{D}{l}\right) = \frac{4}{3\pi}\left[\frac{\sqrt{1+u^2}}{u^2}\big(K(k)-E(k)\big) + \sqrt{1+u^2}E(k) - u\right] \tag{1-6}$$

where $u = D/l$, $k = \sqrt{u^2/(1+u^2)}$, $K(k)$ and $E(k)$ are elliptic integrals of k. It is calculated as L=1.315μH.

Upon theoretical calculation and analysis, we found that the dielectric loss is greater than the ohmic loss of the copper wire and the internal resistance of the varactor. The introduction of the varactor into each unit results in a relatively modest increase in total losses.

We also conducted experimental measurements of the S_{11} for both the single solenoid and the NMA (Supplementary Fig. 1b, using the same characterization method in Supplementary Section S6). Subsequently we calculated their respective quality factors:

$$Q = \frac{\omega_0}{\omega_H - \omega_L} \tag{1-7}$$

where ω_H-ω_L corresponds to the -3 dB bandwidth of the S_{11} curve. The experimental outcomes indicate a similarity between the single solenoid (Q = 60.2) and the NMA (Q = 58.6), with the experimental quality factor of the single solenoid close to the theoretically calculated values ($Q = \omega_0 L/(R_{ohm} + R_{dielec}) = 70.8$).

S2. Fabrication and dimensions of metamaterials

The NMA within nonlinear metamaterials (NLMMs) was primarily fabricated using a combination of 3D printing and copper wire winding, as depicted in Supplementary Fig. 2.

At first, a scaffold was created employing fused deposition modeling (FDM) 3D printing, with PLA serving as the raw material (Supplementary Fig. 2a). Subsequently, 0.6 mm-diameter copper wires were wound along the grooves of the scaffold to form the solenoid (Supplementary Fig. 2b). Since the diminutive size of the varactor (SMV1235-079LF, Skyworks), it was soldered onto a small PCB to expose its pads for connection with the copper wire (Supplementary Fig. 2c). Thereafter, the PCB was soldered into the gap of the split ring to establish a VLSRR (Supplementary Fig. 2d), which was subsequently affixed to a predetermined slot on the 3D printed scaffold to form an NMA (Supplementary Fig. 2e). By controlling the number of NMAs and adjusting their spatial periodicity, the resonant frequency of the NLMMs could be aligned with the MRI's RF operating frequency.

The geometric parameter values of the NLMM are provided in Supplementary Table 1.

S3. Theoretical model of the NMA

We analyzed the resonance response of the NMA in NLMMs by the coupled-mode theory (CMT), specifically, we described the NMA using the one-port-two-resonance CMT model. The CMT model contains the following equations:

$$\frac{d\boldsymbol{a}}{dt} = (j\boldsymbol{\Omega} - \boldsymbol{\Gamma})\boldsymbol{a} + \boldsymbol{k}^{\boldsymbol{T}} s_{+} \tag{3-1}$$

$$s_{-} = \boldsymbol{C} s_{+} + \boldsymbol{d}\boldsymbol{a} \tag{3-2}$$

where $\boldsymbol{a} = [a_1\ a_2]^T$ is the mode amplitudes of each resonance modes, representing the mode amplitude of the VLSRR and solenoid respectively. $\boldsymbol{\Omega}$ is the matrix composed of the resonance frequency and the direct coupling coefficients, $\boldsymbol{\Gamma}$ is the matrix composed of the decay rate and the indirect coupling coefficients, and $\boldsymbol{k}$ is the coupling coefficients between the input port and resonance modes. $s_{+} = |s_{+}|e^{j\omega t}$ is the incident wave, s_{-} represents the wave leaving the resonator, and the relationship between s_{+} and s_{-} is associated by matrices $\boldsymbol{C}$ and $\boldsymbol{d}$. The concrete expressions of above matrices are as follows:

$$\boldsymbol{\Omega} = \begin{bmatrix} \omega_1 & \kappa_{12} \\ \kappa_{12} & \omega_2 \end{bmatrix} \tag{3-3}$$

$$\boldsymbol{\Gamma} = \begin{bmatrix} \gamma_{e1} + \gamma_{o1} & \sqrt{\gamma_{e1}\gamma_{e2}}e^{-j\theta_{12}} \\ \sqrt{\gamma_{e1}\gamma_{e2}}e^{j\theta_{12}} & \gamma_{e2} + \gamma_{o2} \end{bmatrix} \tag{3-4}$$

$$\boldsymbol{k} = \begin{bmatrix} \sqrt{2\gamma_{e1}}e^{j\theta_1} & \sqrt{2\gamma_{e2}}e^{j\theta_2} \end{bmatrix} \tag{3-5}$$

$$C = -1 \tag{3-6}$$

$$\boldsymbol{d} = \boldsymbol{k}^* = \begin{bmatrix} \sqrt{2\gamma_{e1}}e^{-j\theta_1} & \sqrt{2\gamma_{e2}}e^{-j\theta_2} \end{bmatrix} \tag{3-7}$$

where κ_{12} and θ_{12} are the direct coupling coefficient and phase difference between the two modes; ω_i is the resonance frequency, and γ_{ei} and γ_{oi} are the radiation loss and intrinsic loss of each resonance modes. For simplicity, κ_{12} is restricted to a real number, θ_1 is set to 0, and $s_+ = |s_+|$. Thus, $\theta_{12} = \theta_2$.

For ω_1, since the junction capacitance of the varactor is related to the bias voltage across the varactor, the resonant frequency of the VLSRR is related to the resonant amplitude in the VLSRR. Therefore, there is $\omega_1 = (1 - \lambda|a_1|)\omega_{1,0}$, where λ is the first-order nonlinear coefficient. To determine the λ, we consider the VLSRR as a LC resonator so that the ω_1 could be expressed by the following equation:

$$\begin{aligned} \omega_1 &= \frac{1}{\sqrt{LC}} \approx \frac{1}{\sqrt{LC_J(V_R)}} = \frac{1}{\sqrt{LC_{J0}\left(1 + V_R/V_J\right)^{-M}}} \\ &\approx \frac{1}{\sqrt{LC_{J0}}}\left(1 + \frac{M}{2V_J}\right)V_R \end{aligned} \tag{3-8}$$

where C_{J0} is the zero-bias junction capacitance, V_R is the bias voltage, V_J is the junction potential, and M is the grading coefficient. From the datasheet, C_{J0} is 15.85 pF, V_J is 8.78 V, and M is 4.570 of the varactor (SMV1235, Skyworks). Thus, $\lambda = M / (2V_J) =$ 0.260.

For ω_2, since the resonant frequency of the solenoid is const, there is $\omega_2 = \omega_{2,0}$. All parameter values in the CMT model expressions are listed in the Supplementary Table 2. The theoretical results based on these parameters agree well with the simulation and experimental results using these parameters.

By substituting the above equations into Supplementary Equation (3-1) and converting differential equations in the time domain to the frequency domain, the CMT model could be expressed as the following equation:

$$\begin{bmatrix} j\omega a_1 \\ j\omega a_2 \end{bmatrix} = \begin{bmatrix} j(1-\lambda|a_1|)\omega_{1,0} - (\gamma_{e1}+\gamma_{o1}) & jk - \sqrt{\gamma_{e1}\gamma_{e2}}e^{-j\theta_2} \\ jk - \sqrt{\gamma_{e1}\gamma_{e2}}e^{j\theta_2} & j\omega_{2,0} - (\gamma_{e2}+\gamma_{o2}) \end{bmatrix} \begin{bmatrix} a_1 \\ a_2 \end{bmatrix} + \begin{bmatrix} \sqrt{2\gamma_{e1}} \\ \sqrt{2\gamma_{e2}}e^{j\theta_2} \end{bmatrix} |s_+| \tag{3-9}$$

We could obtain the solutions of a_1 and a_2 by solving Supplementary Equation (3-9), and then calculate the reflection coefficient spectra of the NMA using the solutions of a_1 and a_2 through:

$$r = \frac{s_-}{s_+} = -1 + \sqrt{2\gamma_{e1}}\frac{a_1}{|s_+|} + \sqrt{2\gamma_{e2}}e^{-j\theta_2}\frac{a_2}{|s_+|} \tag{3-10}$$

The mode amplitudes spectra and the reflection coefficient spectra are shown in the Fig. 1d-g of the main text.

S4. Numerical simulation method for nonlinearity of metamaterials

We propose an electromagnetic (EM) field-circuit joint simulation process that combines the finite integral method with a simulation model incorporating lumped elements to directly emulate the nonlinearity of resonance in relation to incident power. The schematic of this simulation process is illustrated in Supplementary Fig. 3.

Firstly, we developed a simulation program with integrated circuit emphasis (SPICE) model for the varactor, guided by the datasheet specifications. The SPICE model encompasses a diode, an internal resistance, and an inductance and a capacitance due to the package of the varactor. These components were defined in standard SPICE syntax and subsequently organized in the requisite pin order to create the SPICE model file needed for simulation.

Subsequently, we constructed the simulation model of the NLMM, which comprised 2×2 NMAs, utilizing CST Studio Suite software (Supplementary Fig. 3a). The dimensions of the simulation model matched those of the physical sample described in Supplementary Section S2. The scaffold material of the NMA was modeled as a dielectric with a permittivity of 2+0.06i. To facilitate the direct simulation of nonlinear responses, we introduced a lumped element model representing the varactor within the split ring gap, importing the previously created SPICE model file for the varactor. For reflection coefficient simulations, the model also incorporated a loop antenna with a discrete port, situated at the gap of the loop antenna, responsible for exciting the NLMM resonance. The boundary conditions of the simulation model were configured as open boundaries, in alignment with the characterization setup detailed in Supplementary Section S6.

Next, we employed the time domain solver to simulate the nonlinear response of the NLMM. Following a methodology analogous to experimental reflection spectra measurements, we employed sinusoidal signals as the excitation signal. We monitored both the transmitted signal (designated as i1) and the reflected signal (designated as o1,1) at the discrete port. As depicted in Supplementary Fig. 3b, when the excitation signal's frequency matched the resonant frequency of the NLMM, the NLMM exhibited resonance at lower incident power (-20 dBm) and displayed significant absorption of the incident signal. Conversely, at higher incident power (0 dBm) and at the same excitation frequency, the NLMM no longer exhibited resonance at the previous frequency due to a shift in its resonant response. These simulation results convincingly demonstrate the nonlinear response of the NLMM to incident power.

For data post-processing, we converted the time domain solved results to frequency domain by Fast Fourier Transform (FFT) (Supplementary Fig. 3c). Then we calculated the ratio between the frequency-domain o1,1 and i1 signals to derive the reflection coefficient at specific excitation frequencies and amplitudes. By sweeping the frequency and amplitude of the excitation signal, we generated reflection coefficient spectra at varying incident power levels, as illustrated in Supplementary Fig. 3d. Due to the substantial computational time required for the complete NLMM model, Supplementary Fig. 3d exclusively presents spectra for the VLSRR. These spectra reveal the nonlinear response of the VLSRR's reflection coefficient to excitation power. The comprehensive simulation results for the entire NLMM are presented in the Fig. 2a and 2b of the main text. Notably, the reflection coefficient curves obtained through simulation lack an abrupt discontinuity observed in CMT model calculations. This disparity may be attributed to that the simulation time step length is much smaller than the excitation signal period, and the solver treat the change of the characteristics of the varactor as a slow and continuous process.

We observed the establishment of bias voltage and electric field distribution across the varactor under varying incident power through simulation, as illustrated in Supplementary Fig. 4. Under conditions of low incident power, the voltage drop across the varactor remains consistent during both forward and reverse biasing

(Supplementary Fig. 4a), with the electric field distribution near the split ends exhibiting a symmetrical pattern during both forward and reverse biasing (Supplementary Fig. 4b). As the incident power increases, the reverse bias voltage across the varactor continues to rise (Supplementary Fig. 4c), resulting from a significantly stronger electric field at the cathode during reverse biasing compared to forward biasing (Supplementary Fig. 4d). The joint simulation method effectively integrates the field and lumped element parameters.

Additionally, we employed a similar approach to simulate the spatial distribution of the magnetic field within the NLMM at varying incident power levels, with the objective of analyzing the enhancement effect on the RF magnetic field. Two waveguide ports were positioned on the y-normal boundary for excitation, while the x-normal boundary was configured as a perfect electric conductor, and the z-normal boundary as a perfect magnetic conductor to constrain the direction of the incident magnetic field along the y-axis. All other simulation settings remained unchanged. The outcomes of these simulations are presented in Fig. 2d in the main text.

S5. Theoretical calculation of magnetic field enhancement ratio

We used Faraday's Law and Biot-Savart Law to calculate the magnetic field enhancement ratio attributed to the NLMM, and the calculation process is following.

An alternating and harmonic RF magnetic field $B_{1,0}(t)$ [$B_{1,0}(t) = B_{1,0}\exp(j(\omega t - kz + \varphi_B))$] propagating axially along the NMA causes an induced electromotive force in the solenoid:

$$V = -N\frac{d\Phi}{dt} = -N\left(\frac{\pi D^2}{4}\right)\frac{dB}{dt} \tag{5-1}$$

$$V_p = -j\omega N\left(\frac{\pi D^2}{4}\right)B_{1,0} \tag{5-2}$$

Then the peak value of the induced current in the solenoid is:

$$I_p = \frac{V_p}{Z} \tag{5-3}$$

Since the series impedance of capacitance and inductance in series resonance is zero, the impedance is:

$$Z = (R_{ohm} + R_{dielec}) + j\omega_0 L + \frac{1}{j\omega_0 C} = R_{ohm} + R_{dielec} \tag{5-4}$$

where R_{ohm} and R_{dielec} are ohmic loss and dielectric loss from Supplementary Equation (1-3) and (1-4).

Since the current at the ends of the solenoid is zero, we assume that the current is sinusoidal along the wire and consider the current is maximum at the midpoint of the wire and zero at the ends. The induced current in the solenoid is:

$$I = I_p \sin\left(\frac{\pi l_w}{l_{w,tot}}\right)\exp(j\omega t) \tag{5-5}$$

The above calculation process also could give the induced current in the VLSRR, but assuming that the current is uniformly distributed along the ring, i.e., $I = I_p$.

The magnetic field produced by the current flowing through a micro-segment ds of an arbitrarily shaped wire at the point P at a distance r is calculated by the Biot-Savart Law:

$$d\boldsymbol{B} = \frac{\mu_0}{4\pi} I \frac{d\boldsymbol{s} \times \boldsymbol{r}}{|\boldsymbol{r}|^3} \tag{5-6}$$

Then the magnetic field generated by the whole wire at point P is the sum of the magnetic field generated by each micro-segment ds_i:

$$\boldsymbol{B} = \sum_i d\boldsymbol{B_i} = \frac{\mu_0}{4\pi}\sum_i I_i \frac{d\boldsymbol{s_i} \times \boldsymbol{r_i}}{|\boldsymbol{r_i}|^3} \tag{5-7}$$

Therefore, the magnetic field enhancement ratio at point P is:

$$R_B(P) = \frac{\left|\Sigma\left(\boldsymbol{B_{i,solenoid}} + \boldsymbol{B_{i,VLSRR}}\right) + B_{1,0}\right|}{|B_{1,0}|} \tag{5-8}$$

Supplementary Fig. 5 shows the magnetic field enhancement calculation result along the meta-atom's center axis. The magnetic field enhancement brought by the solenoid part, the VLSRR part, and the sum of the two are given.

S6. Characterization of the resonance frequency of metamaterials

For characterizing the nonlinear response of the NLMM, we measured the S_{11} parameter (i.e., reflection coefficient) of the metamaterial using the vector network analyzer (VNA, N5230C, Agilent).

The experimental setup for S-parameter measurements is shown in Supplementary Fig. 6a. We connected a loop antenna to one of the ports of the VNA for excitation. Then we measured the S_{11} at different excitation power ranging from -30 dBm to +5 dBm. According to the test results (Supplementary Fig. 6b), the resonance frequency of the NLMM was about 124 MHz at -30 dBm power. As the excitation power increased, the S_{11} spectra shifted to the lower frequency and had the abrupt jump point, consistent with the CMT model.

Furthermore, to investigate the effect of the imaging samples on the resonant frequency and nonlinear response of the NLMM, we measured the S_{11} of the NLMM under the bottle-shaped phantom loaded. The phantom was filled with edible oil (5S first-grade pressed peanut oil, Luhua) and water solution (3.75 g $NiSO_4 \times 6H_2O$, 5 g NaCl/ 1 kg H_2O, Siemens Healthcare), respectively. The experimental setup is shown in Supplementary Fig. 6c. Measurement results (Supplementary Fig. 6d) show that the resonance frequency of the NLMM shifts to the lower frequency after loading the phantom. On the other hand, the presence of the phantom also decreases the quality factor of the NLMM. Notably, the water-based phantom induced more significant changes in both the resonance frequency and the quality factor compared to the oil-based phantom.

These observations can be attributed to differences in the dielectric properties of the substances within the phantom. An equivalent capacitance exists between the metamaterial and the phantom, causing the shift in resonance frequency. Since the permittivity of water is greater than that of oil, it leads to a larger equivalent capacitance and, consequently, a more pronounced frequency shift. On the other hand, the decrease in the quality factor is due to eddy current losses in the phantom. Given that the resistivity of the water solution is lower than that of oil, the water phantom induces a more substantial reduction in the quality factor.

To characterize the performance of the NLMM more directly, the phantom filled with edible oil is used in the MRI validation.

S7. MRI validation

We performed the MRI experiments on the MAGNETOM Prisma 3T MRI

(Siemens Healthcare) to validate the effect of the NLMM in the SNR enhancement. We placed the Body 18 surface coil array (Siemens Healthcare) on the patient bed of the MRI system, and the NLMM on the coil. An acrylic holder mechanically adjusted the gap between the metamaterial and the surface coil to regulate the coupling strength to find the optimal coupling effect.

For imaging with phantoms, we placed the phantom on top of the NLMM, maintaining a separation distance of approximately 4 mm. The imaging sequence employed in these experiments was the FLASH sequence, with the corresponding parameter values detailed in Supplementary Table 3. The RF transmission was carried out using the body coil, while the coil Body 18 served as the receiver for RF signals.

The measured SNR was calculated by:

$$\mathrm{SNR} = \frac{\mu_{signal}}{\sigma_{noise}} \qquad (7\text{-}1)$$

wherein the background of the MRI image at the position far away from the phantom region was taken as the noise to calculate the standard deviation as the σ_{noise}. And the phantom region at different heights was sliced to calculate the mean value as the μ_{signal} along the height direction of the phantom.

Before the MRI validation experiment, we conducted a preliminary experiment to locate the NLMM on the coil Body 18. Firstly, we conducted MRI scanning of a large phantom that covered approximately 1/3 of the coil Body 18 coil. The imaging results of the phantom placed at different positions on the surface coil array are illustrated in Supplementary Fig. 7a. In Supplementary Fig. 7a, the signal intensity near the green dotted line appears higher, indicating the area where the coil elements overlap[S5]. Further experimental tests found that regardless of the NLMM's position on the surface coil array, the SNR after NLMM enhancement was almost consistent (Supplementary Fig. 7b and 7c).

Therefore, in the MR imaging with the NLMM enhanced surface coils, we chose to place the NLMM and phantom at the position along the green line on the surface coil (Supplementary Fig. 7a), with a more optimal baseline and more conservative estimation for SNR enhancement ratio.

For the sample imaging of an apple, we placed an apple on the NLMM and utilized the TSE pulse sequence. The parameter values of TSE sequence are given in Supplementary Table 4. For the in vivo sample imaging, we scanned volunteers' lower legs using the TSE pulse sequence. The parameter values of TSE sequence are given in Supplementary Table 5.

S8. Verification of the nonlinearity on MRI and SAR simulation

We verified the nonlinearity of the NLMM on the MRI platform. We conducted phantom imaging with different flip angle (FA) settings, while other imaging parameters remained consistent with those in Supplementary Section S7. When evaluating the mean signal in the region at the bottom of the phantom, the variations in the signal and nominal FA with and without the NLMM exhibited the same trend, as shown in Supplementary Fig. 8a. The Ernst angle is about 67° both with and without the metamaterials, indicating that the T1 of the oil phantom is approximately 110 ms.

Then we used the dual-angle method to measure the FA map. Ideally, we expect the NLMM not to enhance the RF transmission field, as indicated by the measured FA being equal to the set value in the presence of the NLMM. The specific method is to acquire two images with FAs of α and 2α respectively, while keeping other imaging parameters to be the same. The signal values at the same pixel of the two images are:

$$S_1 = M_0 \sin\alpha \tag{8-1}$$

$$S_2 = M_0 \sin 2\alpha \tag{8-2}$$

Thus, the FA at the pixel is:

$$\alpha = \arccos\frac{S_2}{2S_1} \tag{8-3}$$

Notably, when measuring the FA using the dual-angle method, it is necessary to make the magnetization vector recover completely after each excitation, i.e., set TR> T1. The experiment measured two images with TR= 500 ms and FAs of 35° and 70°, respectively.

The measurement results are shown in Supplementary Fig. 8b. We observed a local increase in the FA near the lower right surface of the phantom, with a maximum increase of 6.3°, indicating that the NLMM has some effect on the transmission field. However, this impact is not significant. When calculating the average FA within a 20×12 mm region, it increased by 2.1° to reach 37.1°. Therefore, we concluded that while our NLMM does have some impact on the RF transmission field, the primary improvement in SNR still results from enhancing the RF reception field.

On the other hand, due to the NLMM's impact on the RF transmission field, we further evaluated its effect on RF safety. Generally, although the maximum FA increased by 6.3°, indicating a rise in specific absorption rate (SAR) values, the increase in FA is not significant on average and the heating effect caused by the NLMM will be minimal due to tissue thermal conductivity.

We evaluated the SAR using simulation. The simulation model is shown in Supplementary Fig. 8c. We modeled the birdcage coil resonating at the 3 T Larmor frequency, inspired by the MRI system routine in CST Studio Suite (provided by Biometrics and Medical Informatics, Otto von Guericke University Magdeburg, Germany), but with different sizes and capacitance values. We modeled a lossy phantom filled with tissue-simulating fluid (ε_r=20, Electric conductivity = 1 S/m) of the same dimensions as used in the MRI validation experiment. Then, we imported the NLMM model detailed in Supplementary Section S4. We set the $B_1^+{}_{rms}$ produced by the birdcage coil to 1 μT[6], and the simulated SAR results with and without the NLMM are shown in Supplementary Fig. 8d. We observed that with the presence of the NLMM, the maximum SAR value increased by a factor of 1.12 (0.753/0.674), and the local average value increased by a factor of 1.12 (0.632/0.565). These results indicate that the SAR increase remains within safety standards[7]. Additionally, simulations revealed that with the NLMM, RF power deposition occurs on one side, which is related to the polarization direction of the circularly polarized field generated by the birdcage coil. Changing the polarization direction alters the side of RF power deposition.

Reference

1. Duan, G., Zhao, X., Anderson, S. W. & Zhang, X. Boosting magnetic resonance imaging signal-to-noise ratio using magnetic metamaterials. *Commun. Phys.* **2**, 35 (2019).
2. Zhao, X., Duan, G., Wu, K., Anderson, S. W. & Zhang, X. Intelligent Metamaterials Based on Nonlinearity for Magnetic Resonance Imaging. *Adv. Mater.* **31**, 1905461 (2019).
3. Maxwell, J. C. *A Treatise On Electricity and Magnetism (Vol. 2)*. vol. 2 (Dover Publications Inc, Mineola, New York, 1954).
4. Nagaoka, H. The Inductance Coefficients of Solenoids. *Journal of the College of Science, Imperial University, Tokyo* **27**, 33 (1909).
5. McGee, K. P. *et al.* Characterization and evaluation of a flexible MRI receive coil array for radiation therapy MR treatment planning using highly decoupled RF circuits. *Phys. Med. Biol.* **63**, 08NT02 (2018).
6. Yao, A., Li, Z. & Ma, M. Impact of MRI RF coil design on the RF-induced heating of medical implants: fixed $B_1^+{}_{rms}$ exposure versus normal operating mode. *Phys. Med. Biol.* **69**, 055021 (2024).
7. McRobbie, D. W., Moore, E. A. & Graves, M. J. *MRI from Picture to Proton*. (Cambridge University Press, West Nyack, 2017).

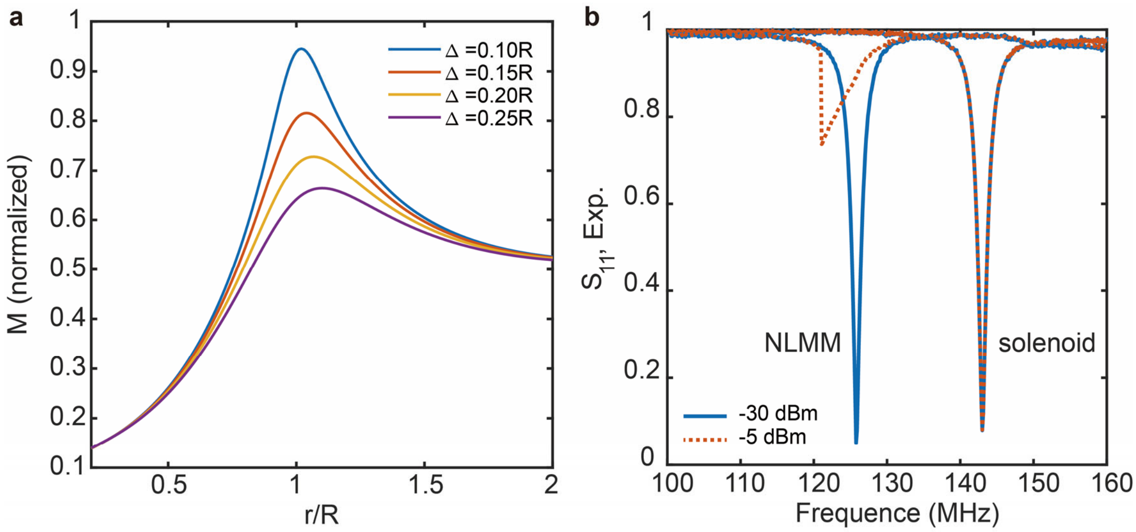

Supplementary Fig. 1 | Estimation results to illustrate the design decisions of the nonlinear meta-atom (NMA). a Calculation results of the mutual inductance between two coaxial loops. **b** Experimental S_{11} measurements of the single solenoid and the NMA.

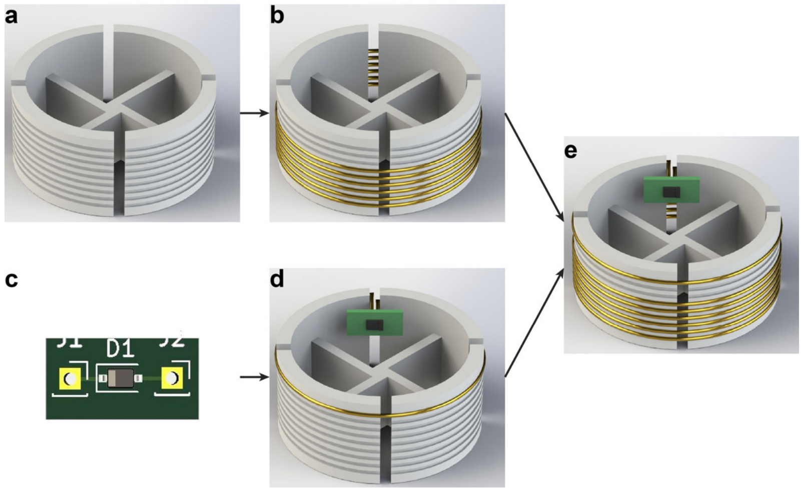

Supplementary Fig. 2 | Fabrication process of the metamaterials. a 3D printing the scaffold; **b** Winding the solenoid along the grooves on the scaffold; **c** Fabricating the PCB for leading out the varactor solder pads; **d** Winding and soldering the VLSRR; and **e** Forming the NMA.

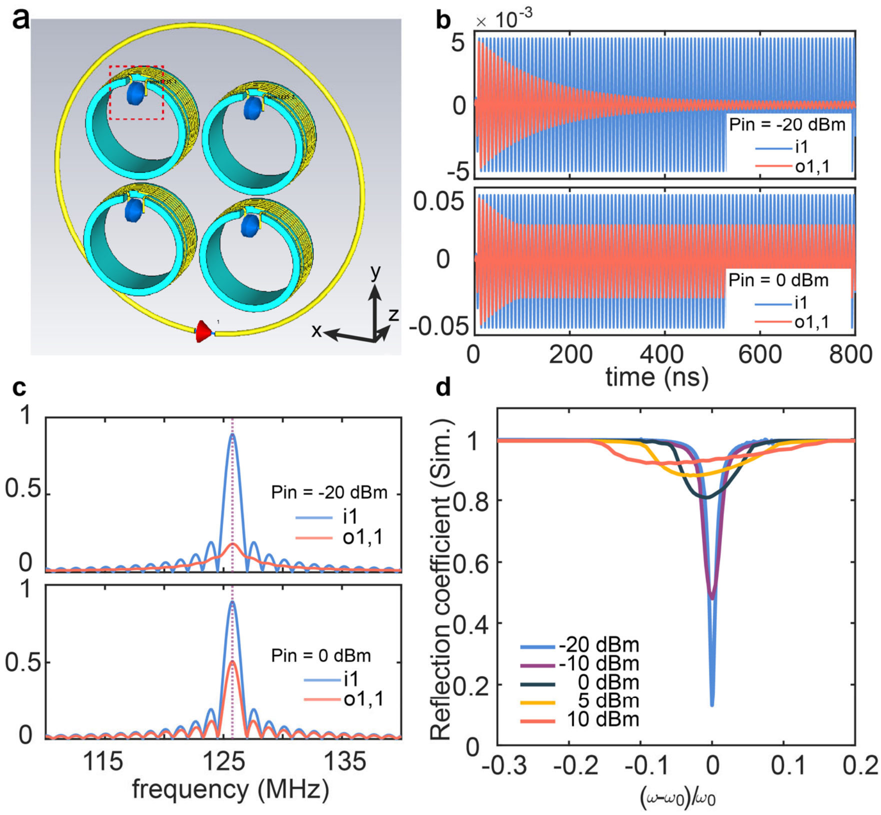

Supplementary Fig. 3 | Electromagnetic (EM) Field-circuit joint simulation process and simulated reflection spectrum. a Simulation model in CST software, including an excited loop antenna and 2×2 NMAs. The lumped element is the SPICE model of the varactor. **b** Time domain solver results at the same excitation frequency but different incident power. i1 and o1,1 represent the transmitting and receiving signal of the excitation port respectively. **c** Frequency domain results obtained by the Fourier transform of time domain results. **d** The reflection coefficient spectra curve simulated by scanning the amplitude and frequency of the excitation signal.

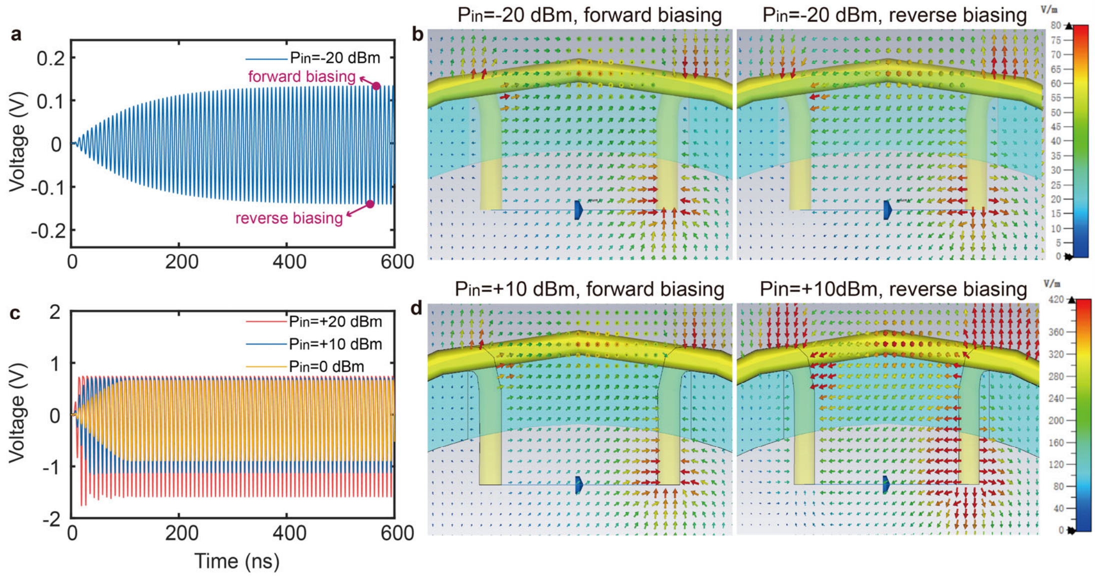

Supplementary Fig. 4 | Simulation of bias voltage establishment and electric field distribution across the varactor. a, c Temporal domain process of bias voltage establishment across the varactor under varying incident power. **b, d** Comparison of the electric field distribution around the split ends during the peak of forward and reverse biasing occurrences.

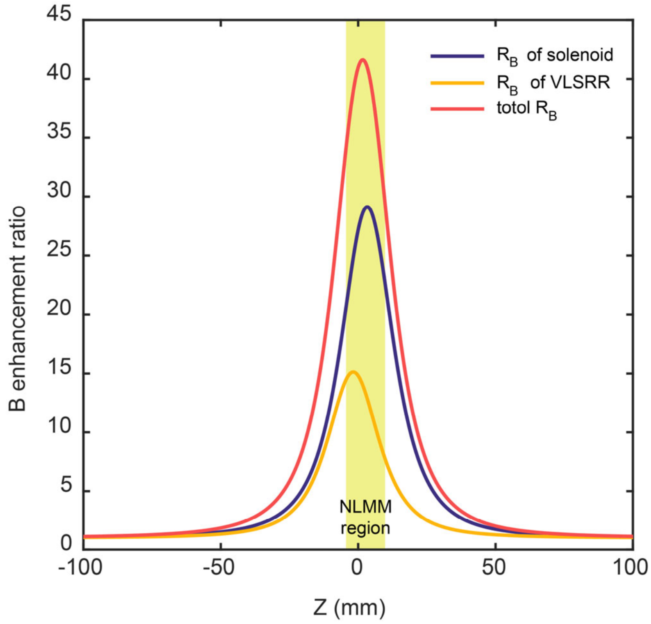

Supplementary Fig. 5 | Theoretical calculation results of magnetic field enhancement ratio, includes magnetic field enhancement from solenoid and VLSRR, respectively, as well as the overall magnetic field enhancement ratio.

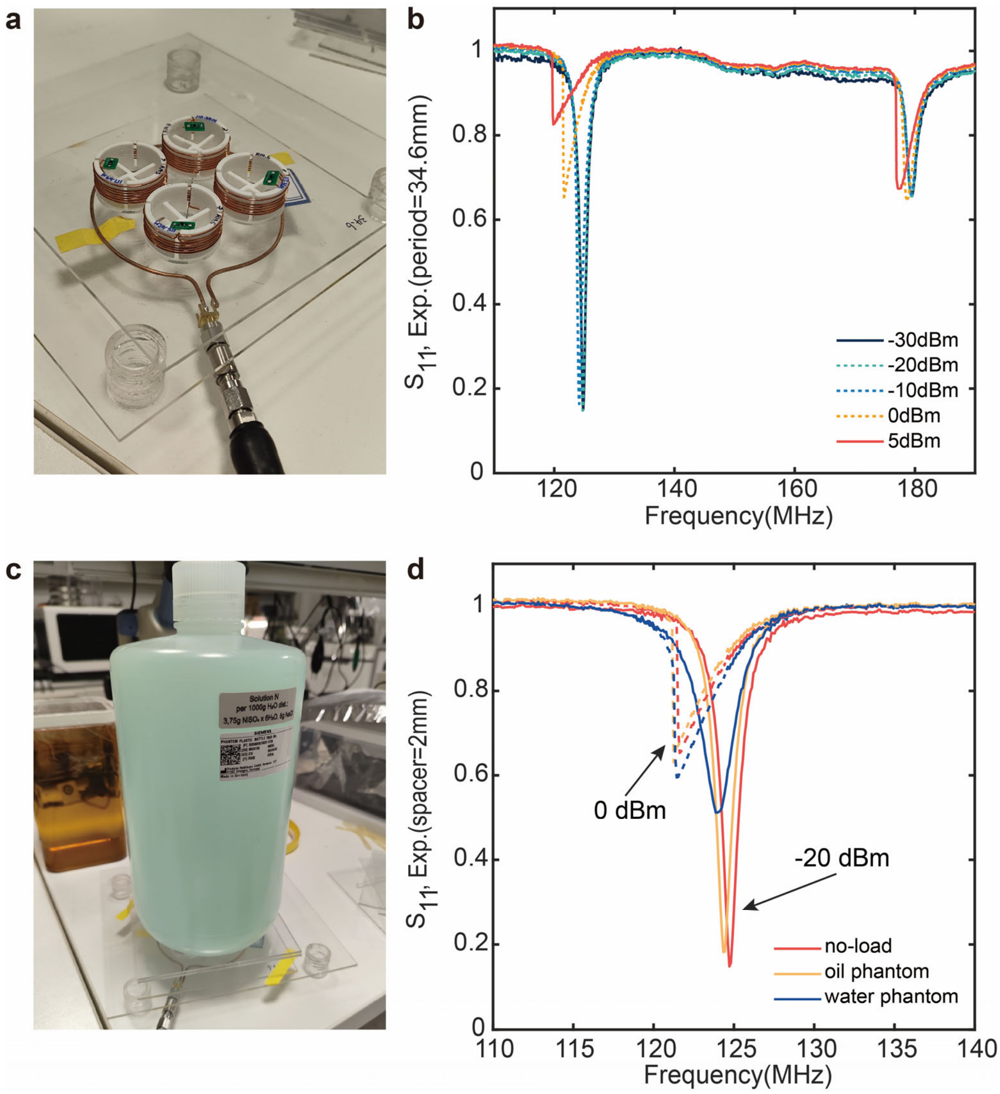

Supplementary Fig. 6 | S_{11} measurements of the metamaterial. a Experimental setup where the loop antenna was connected to the VNA port for excitation. **b** S_{11} measurement results under different excitation powers. **c** Experimental setup where the phantom was placed on the NLMM; **d** S_{11} measurement result under different material loading, where the solid line is the measurement at excitation power -20 dBm and the dotted line is the measurement at excitation power 0 dBm.

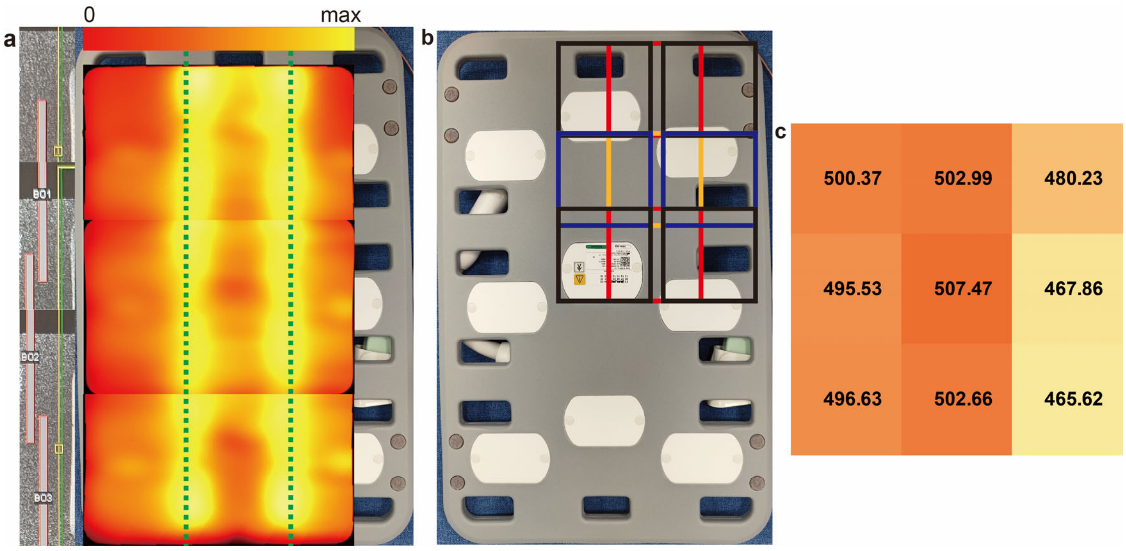

Supplementary Fig. 7 | Preliminary experiment to determine the position of the metamaterial relative to the coil. a Images of a large phantom positioned at three different locations on the surface coil array, including the coil positioning illustrated in the MRI scanner software (BO1, BO2 and BO3 on the left). **b** Placement of the metamaterial and the phantom at nine different positions (represented by different colored boxes) on the surface coil, with corresponding calculation of SNR (**c**).

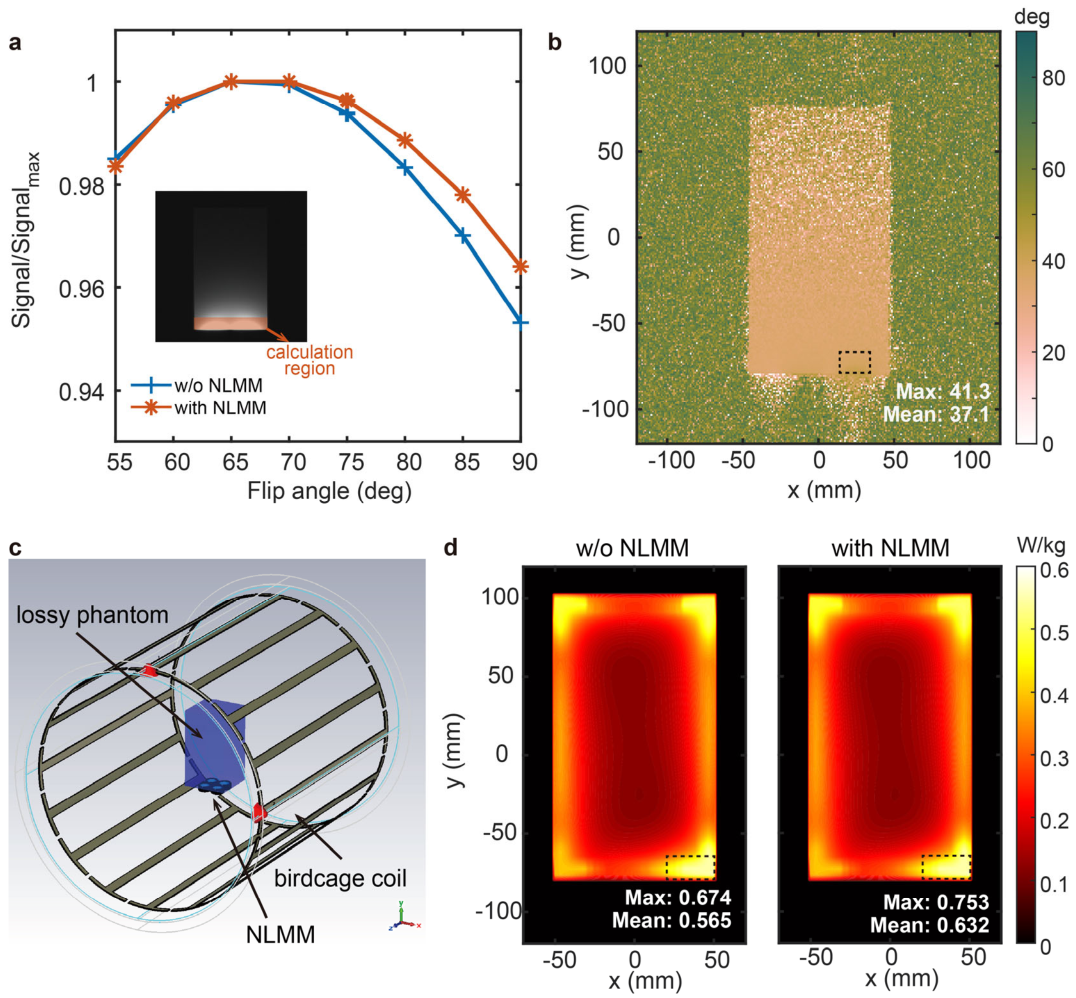

Supplementary Fig. 8 | Validation of the nonlinearity of the NLMM through MRI experiments and SAR simulation. **a** Mean signal intensity variation corresponding to different flip angles (FAs) with a TR of 100 ms, comparing cases with and without the NLMM. The calculation region is employed to calculate the mean signal. **b** Measured results of FA during imaging using the surface coil with the NLMM, obtained through the double-angle method with FAs of 35° and 70°, with a TR of 500 ms. **c** Simulation model to evaluate SAR. **d** Simulated SAR maps of the phantom without (left) and with the NLMM (right).

Supplementary Table 1 | The geometric parameter values of the NLMM

Parameter	Value	Description
D	29 mm	outside diameter of the scaffold
d	0.6 mm	diameter of the copper wire
p	1.2 mm	pitch of the solenoid
N	5.5	number of turns of the solenoid
l	$l = p \times N$ = 6.6 mm	length of the solenoid
$l_{w,tot}$	$l_{w,tot} = \sqrt{l^2 + (N\pi D)^2} = 0.5\ m$	copper wire length of solenoid
dis	1.2 mm	distance between the solenoid and the VLSRR in the NMA
spa	34.6 mm	spatial period of NMAs

Supplementary Table 2 | The parameter values in the CMT model of the NMA

Parameter	Value
γ_{e1}	$3.821\times 10^{6}(s^{-1})$
γ_{o1}	$4.907\times 10^{6}(s^{-1})$
γ_{e2}	$5.200\times 10^{6}(s^{-1})$
γ_{o2}	$8.053\times 10^{6}(s^{-1})$
$\omega_{1,0}$	$8.363\times 10^{8}(rad \cdot s^{-1})$
$\omega_{2,0}$	$9.117\times 10^{8}(rad \cdot s^{-1})$
λ	0.260
k	$0.15\omega_{1,0}$
θ_2	0.8π

Supplementary Table 3 | Parameter Settings of FLASH pulse sequence

Parameter	Value
Matrix size	256×256 mm
Pixel size	1×1 mm
Slice thinness	2 mm
TR	100 ms
TE	4.62 ms
Flip angle	70 deg

Supplementary Table 4 | Parameter Settings of TSE pulse sequence of the apple imaging

Parameter	Value
Matrix size	180×180 mm
Pixel size	0.47×0.58 mm
Slice thinness	3 mm
TR	7970 ms
TE	89 ms
Flip angle	150 deg
Phase oversampling	30%
Turbo factor	17

Supplementary Table 5 | Parameter Settings of TSE pulse sequence of the human lower leg imaging

Parameter	Value
Matrix size	140×140 mm
Pixel size	0.3×0.3 mm
Slice thinness	3 mm
TR	4000 ms
TE	67 ms
Flip angle	150 deg
Phase oversampling	0%
Turbo factor	14